A multiwavelength study of the highly asymmetrical debris disk around HD 111520

Crotts, Katie A.; Draper, Zachary H.; Matthews, Brenda C.; Duchêne, Gaspard; Esposito, Thomas M.; Wilner, David; Mazoyer, Johan; Padgett, Deborah; Kalas, Paul; Stapelfeldt, Karl

Publisher's version / Version de l'éditeur:
https://doi.org/10.3847/1538-4357/ac6c86
The Astrophysical Journal, 932, 1, 2022-06-10

The Astrophysical Journal, 932:23 (11pp), 2022 June 10 https://doi.org/10.3847/1538-4357/ac6c86

A Multiwavelength Study of the Highly Asymmetrical Debris Disk around HD 111520

Katie A. Crotts[1], Zachary H. Draper[1,2], Brenda C. Matthews[2], Gaspard Duchêne[3,4], Thomas M. Esposito[3,5], David Wilner[6], Johan Mazoyer[7], Deborah Padgett[8], Paul Kalas[3,5,9], and Karl Stapelfeldt[8]
[1] Physics & Astronomy Department, University of Victoria, 3800 Finnerty Road, Victoria, BC, V8P 5C2, Canada; ktcrotts@uvic.ca
[2] Herzberg Astronomy and Astrophysics, National Research Council of Canada, 5071 West Saanich Road, Victoria, BC V9E 2E7, Canada
[3] Astronomy Department, University of California, Berkeley, CA 94720, USA
[4] Université Grenoble Alpes/CNRS, Institut de Planétologie et d'Astrophysique de Grenoble, F-38000 Grenoble, France
[5] SETI Institute, Carl Sagan Center, 189 Bernardo Avenue, Mountain View CA 94043, USA
[6] Center for Astrophysics—Harvard & Smithsonian, 60 Garden Street, Cambridge, MA 02138, USA
[7] LESIA, Observatoire de Paris, Université PSL, CNRS, Sorbonne Université, Université de Paris, 5 place Jules Janssen, F-92195 Meudon, France
[8] Jet Propulsion Laboratory, California Institute of Technology, 4800 Oak Grove Drive Pasadena, CA 91109 USA
[9] Institute of Astrophysics, FORTH, GR-71110 Heraklion, Greece
Received 2022 January 18; revised 2022 April 29; accepted 2022 May 2; published 2022 June 13

Abstract

We observed the nearly edge-on debris disk system HD 111520 at the *HJ* and *K*1 near-infrared (NIR) bands using both the spectral and polarization modes of the Gemini Planet Imager. With these new observations, we have performed an empirical analysis in order to better understand the disk morphology and its highly asymmetrical nature. We find that the disk features a large brightness and radial asymmetry, most prominent at shorter wavelengths. We also find that the radial location of the peak polarized intensity differs on either side of the star by 11 au, suggesting that the disk may be eccentric, although, such an eccentricity does not fully explain the large brightness and radial asymmetry observed. Observations of the disk halo with the Hubble Space Telescope also show the disk to be warped at larger separations, with a bifurcation feature in the northwest, further suggesting that there may be a planet in this system creating an asymmetrical disk structure. Measuring the disk color shows that the brighter extension is bluer compared to the dimmer extension, suggesting that the two sides have different dust grain properties. This finding, along with the large brightness asymmetry, are consistent with the hypothesis that a giant impact occurred between two large bodies in the northern extension of the disk, although confirming this based on NIR observations alone is not feasible. Follow-up imaging with the Atacama Large Millimeter/submillimeter Array to resolve the asymmetry in the dust mass distribution is essential in order to confirm this scenario.

Unified Astronomy Thesaurus concepts: Debris disks (363); Circumstellar disks (235); Near infrared astronomy (1093); Polarimetry (1278)

1. Introduction

Debris disks are optically thin, dust disks around stars, which are generated through the perturbation of planetesimals in the system. This causes what is known as a *collisional cascade* of larger bodies that produces micron- to millimeter-sized dust grains (Wyatt 2008; Macintosh et al. 2014; Hughes et al. 2018). As instrumentation has improved over the last decade, allowing for higher resolution imaging, debris disks have been found to harbor many types of asymmetries and structures such as gaps, rings, eccentricities, brightness asymmetries, and warps (Hughes et al. 2018 and references therein). While such features are often thought to be caused by planets, other mechanisms such as an interaction with the interstellar medium (ISM; Debes et al. 2009) or giant impacts can shape debris disks as well. For example, an ISM interaction was originally thought to have formed the moth- and needle-like halos of the debris disks around HD 61005 and HD 11515 (Rodigas et al. 2012; Schneider et al. 2014), while the brightness asymmetry and CO clump in the southwest extension of β Pic can be explained by a recent massive impact (Dent et al. 2014; Apai et al. 2015). Additionally, the majority of resolved debris disk systems have no known planet companions to directly connect with the disk morphology, demonstrating the need for a more comprehensive understanding of how debris disks are perturbed.

Due to the response of the dust component of debris disks to dynamical perturbations, they are good indicators of a planet's stability, where dust belts can serve as indicators for planetary upheaval by large planetary perturbations or whether minor sculpting could be occurring (Esposito et al. 2016; Marino et al. 2017). Through dynamical modeling, it has been shown that even a single 10 $M_{\oplus}$ planet on an eccentric orbit can produce many different debris disk morphologies and asymmetries (Lee & Chiang 2016). In some cases disk structure can be directly traced to a known planet sculpting the disk such as in the case of β Pic (Mouillet et al. 1997; Dawson et al. 2011; Apai et al. 2015). Another example of this is the asymmetrical debris disk HD 106906, which exhibits both a brightness asymmetry and eccentricity (Kalas et al. 2015; Lagrange et al. 2016; Crotts et al. 2021). Through empirical analysis, these asymmetries are shown to be likely due to the 11 $M_{\rm Jup}$ planet in the system that orbits outside of the disk, and unlikely to be due to an ISM interaction (Crotts et al. 2021). While both β Pic and HD 106906 have known planetary companions, there are other highly asymmetrical debris disks in which no known planets exist. One example is the debris disk HD 160305, recently discovered in 2019, which harbors a large azimuthal brightness

Table 1
Summary of the Data Used in this Paper

Band	Mode	Date	N	$t_{\rm int}$ (s)	ΔPA (°)	MASS Seeing (″)
J	Pol	2016 Mar 26	58	3480	39.1	0.82
J	Spec	2016 Mar 27	51	3060	29.5	0.45
H	Pol	2016 Mar 18	26	2840	28.3	0.48
H	Spec	2015 Jul 2	41	2446	34.8	0.28
$K1$	Pol	2016 Mar 28	36	2160	35.8	1.33
$K1$	Spec	2016 Mar 24	30	1800	19.2	0.59

Note. The H Spec data is the same data from Draper et al. (2016), while the H Pol data (previously published in Esposito et al. 2020) was a subsequent longer observation (582 s versus 2840 s integration time). Here, N = the number of frames, $t_{\rm int}$ = the total integration time in seconds, and ΔPA = the total parallactic angle rotation in degrees.

asymmetry accredited to either a hidden planet companion or a recent large impact (Perrot et al. 2019). Studying highly perturbed debris disks can therefore offer insight into the stirring mechanisms of dust belts, and whether their morphologies were produced by planets in the system or through other phenomena.

HD 111520 (HIP 62657) is located 108.1 ± 0.2 pc from the Sun (Gaia Collaboration et al. 2021) and is a member of the Lower Centaurus Crux group within the Scorpius-Centaurus Association (de Zeeuw et al. 1999). As part of the GPIES campaign (Macintosh et al. 2018, 2014, 2008), which resolved 26 debris disks in polarized and total intensity (Esposito et al. 2020), one of the systems observed was HD 111520. The debris disk was detected in the H band and revealed a strongly asymmetric disk morphology from 0.″3 to 1″, with a 2:1 brightness asymmetry and radial asymmetry measured between the two sides of the disk (Draper et al. 2016). From Hubble Space Telescope (HST) observations, the system had previously been shown to have an asymmetric, *needle*-like disk structure out to 6″ (∼650 au) relative to the central star, along with an even larger 5:1 brightness asymmetry and a bifurcation feature in the northern extension (Padgett & Stapelfeldt 2015). Such a strong asymmetry could be the result of two main scenarios, either the dust grain properties are significantly different between the two extensions, which changes the dust scattering efficiency, or the planetesimal belt itself is being perturbed by dynamical activity, such as that which could result from an unseen planetary companion.

Since HD 111520 is such an unusual system, we have obtained multiwavelength Gemini Planet Imager (GPI) data to better characterize the disk morphology and further investigate its observed asymmetry. We have conducted an empirical analysis of our GPI data through measuring the disk structure in Section 3.1, as well as the surface brightness profiles of each band and disk color in Section 3.2. We then discuss possible explanations for the disk's asymmetries based on the results of our empirical analysis in Section 4.

2. Observations and Data Reduction

The imaging of HD 111520 from GPI was collected over a range of nights, combining data sets from the GPIES survey in the H band (∼1.65 μm; PI: B. Macintosh) and the Debris Disk Large and Long Program in the J and $K1$ bands (∼1.24 and ∼2.05 μm; PI: C. Chen). Observations were taken in both polarimetric and spectroscopic modes, with a field of view (FOV) of 2.″8 × 2.″8 and a pixel scale of 14.166 ± 0.007 mas lenslet^{-1} (De Rosa et al. 2015). A summary of the observations is presented in Table 1. In general, the observations were scheduled to maximize field rotation as the source transited the meridian, with a total observing sequence of around an hour (including overheads) with a series of 60 s exposures to optimize point-spread function (PSF) subtraction. The H-band polarization mode data set, previously published in Esposito et al. (2020), is a longer integration time than the data presented in Draper et al. (2016), therefore achieving a higher signal-to-noise ratio (S/N), comparable to the other bands.

The data reduction in general followed standard practices for GPI data employed by the GPI pipeline (Perrin et al. 2014, and references therein). The polarization mode (pol-mode) is observed as two orthogonal polarization states on the detector and is modulated by an achromatic half-wave plate (HWP) to four different orientations (Perrin et al. 2015). The relative measurement of flux between them can later be used to derive the Stokes parameters in the FOV. The detector images are dark subtracted and *destriped* with a Fourier filter to remove a standing wave pattern from microphonic noise (Ingraham et al. 2014). The flexure in the instrument is compensated using a cross-correlation algorithm to match the detector with the expected positions (Draper et al. 2014). The extracted spot fluxes create the pol-mode data cube and can then be cleaned for bad pixels and systematic offsets using a modified double difference algorithm (Perrin et al. 2014). A geometric distortion correction in the FOV from astrometric standards is then used (Konopacky et al. 2014). The instrumental polarization is also removed based on measurements of the flux under the coronagraph (Millar-Blanchaer et al. 2015). Additionally, the data are smoothed by a Gaussian with a FWHM of 1 pixel. The data were then flux calibrated by measuring the satellite spots produced by GPI's optics with elongated apertures (since the spots are smeared out by diffraction with wavelength in the broad band pol-mode) and compared to Two Micron All Sky Survey (2MASS) JHK magnitudes of the star to calibrate the flux within the data cube (Hung et al. 2015). The spots are also used to determine the star center by using a Radon transform algorithm (Wang et al. 2014; Perrin et al. 2015). The data set at multiple position angles and HWP orientations are then combined with a singular value decomposition on Mueller matrices to create a Stokes data cube. The values are converted to a radial Stokes convention to put the stellocentric polarized emission into a single Stokes mode (Q_ϕ) (Schmid et al. 2006).

In the case of the spectroscopic mode, again standard GPI pipeline data reduction practices are used (Perrin et al. 2014). Each of the individual dispersed light frames were dark subtracted, had bad pixels masked, and were destriped from microphonics (Ingraham et al. 2014). Wavelength calibrations are done using Ar lamp exposures in each respective band

(Wolff et al. 2014). Calibration sources are measured prior to the observing sequence, minimizing flexure offsets. For the J and H bands a standard box aperture method is used to extract the flux into a wavelength calibrated data cube (Maire et al. 2014). In the $K1$ band, the satellite spots had weaker flux compared to the background, which interferes with the calibrations necessary after cube extraction. The microlens PSF extraction method was then used to extract the data from the detector (Draper et al. 2014; Ingraham et al. 2014). The S/N improved enough for the pipeline to find the satellite spots in subsequent steps in at least the central wavelength slice of each $K1$-band integral field spectrometer (IFS) cube. Sky subtraction at the 2D detector was attempted but this step appeared to introduce more noise. The sky subtraction was therefore left to PSF subtraction at later steps using pyKLIP (Wang et al. 2015). For bad spaxel mitigation, a bad pixel identifier and smoothing was applied similar to Draper et al. (2016). The satellite spots were then identified by centering on a high pass filtered image of the data. A best guess position for a slice with high S/N was identified by eye once for the whole sequence to aid the spot location algorithm. The unfiltered images then had their satellite spots extracted to measure the stellar spectrum convolved with the instruments' response function in wavelength and time. The spectrum of each cube was calibrated by comparing the measured flux with the 2MASS magnitude for each respective band. A color correction was applied by comparing the measured spectrum to a real, atlas template spectrum (Pickles 1998) for a star of HD 111520's spectral type (F5V). These two factors essentially measure the flux conversion factors for each cube so that the satellite spots have the same absolute flux and spectra as an F5V star. This calibrates the data in the cube to physically relevant units of Janskys. This algorithm was tested on a known white dwarf spectrum in Maire et al. (2014) and found to be within a 5% flux error with on-sky observations. The reduced data cubes are then run through the program, pyKLIP, which utilizes angular-differential imaging and subtracts the stellar PSF to remove additional flux from the star. For a more in-depth description of this process, we refer to Draper et al. (2016). The final images resolving the disk on both polarized and total intensity can be seen in Figure 1. Additionally, we also include the S/N of our polarized intensity data, which is generated by dividing the Q_ϕ images by noise maps derived from the U_ϕ images. To create these noise maps, we use U_ϕ to calculate the standard deviation at each radius in 1-pixel wide stellocentric annuli. Here, we are assuming that U_ϕ contains no disk signal, which would be expected for an optically thin debris disk causing single scattering.

To better understand the prior HST results, we reprocessed the archival Space Telescope Imaging Spectrograph (STIS) data from GO 12998 (PI: Padgett). HD 111520 was acquired behind the WEDGEA1.0 mask position and imaged in two consecutive orbits with two different roll angles separated by 32°. Each orbit accumulated five 419 s integrations. PSF subtraction was accomplished by differencing the two calibrated and registered _sx2.fits images from each other. The two PSF-subtracted images were rotated to the north and the data were averaged.

3. Observational Analysis

To better understand the disk morphology and asymmetry, we perform an empirical analysis on our multiwavelength GPI data. This includes measuring the vertical structure through the disk FWHM and the vertical offset from the star (i.e., the location of the disk spine), as well as measuring the surface brightness in each band. Characterizing the disk morphology allows us to probe the cause of the observed asymmetries, as different disk perturbers affect the disk differently. For example, interaction with a planet companion may cause structures in the disk geometry such as warps and eccentricities, whereas an interaction with the ISM or a giant impact may cause an asymmetry in the dust grain properties creating an asymmetrical disk color. These results will be further discussed in the context of possible disk perturbers in Section 4.

3.1. Vertical Structure

To measure the vertical structure, we fit a 1D Gaussian profile to the vertical surface brightness profile at a series of radii from the star. As the disk structure should not vary significantly within our small wavelength range, we choose to focus this analysis mainly on the H band, as it has the best S/N, but also perform the analysis on the J and $K1$ bands in order to compare. Additionally, we utilize the polarized intensity data, as we believe it most accurately represents the true disk structure, without the biases introduced by angular differential imaging (ADI)-based PSF subtraction employed for the total intensity data.

We first prepared the data by rotating our data by 75° clockwise, as similarly done in Draper et al. (2016). The data are then binned into 2×2 pixel bins, and additional smoothing using a Gaussian with $\sigma = 2$ pixels ($0\farcs028$) is applied. This is done to increase the S/N and ensure a good fit to the data. Once the Gaussian profile is fit to vertical surface brightness slices along the entire disk using a nonlinear least squares fit, the mean value, and FWHM, along with 1σ uncertainties of each Gaussian fit are extracted. The mean value (i.e., the center of the Gaussian) represents the disk spine, or more specifically, the vertical offset from a horizontal line passing through the star, whereas the FWHM represents the approximate vertical width of the disk. The resulting FWHM and vertical offset profiles for all three bands can be seen in Figure 2. We are able to detect the emission in the H band out to $\sim 1''$ on either side of the disk. While the $K1$ band is also detected symmetrically (although only out to $0\farcs8$ given the lower S/N), the J band does show a radial asymmetry where the southeast (SE) extension is detected out to $\sim 1''$, and the northwest (NW) extension is detected to $\sim 1\farcs1$, which corresponds to a difference of 11 au.

Taking the weighted mean of the H-band FWHM profile, we find the disk to have an approximate FWHM of $0\farcs18$. This is much greater than the GPI's instrumental H-band PSF FWHM of $0\farcs05$, showing that the disk is well resolved. However, this instrumental PSF and any smoothing/binning of the data must be taken into account in order to obtain an intrinsic measurement for the FWHM. This is done by subtracting in quadrature the FWHM of the instrumental PSF, as well as the FWHM of any smoothing applied, from the measured FWHM. Doing so, we obtain an intrinsic FWHM of $0.12 \pm 0\farcs1$ for the J and H bands, and $0.14 \pm 0\farcs1$ for the $K1$ band (13–15 au), which leads to a aspect ratio of ~ 0.28 at 50 au. This aspect ratio is intermediate between similar measurements at 50 au for other near edge-on debris disks such as HD 32297 (0.17; Duchêne et al. 2020) and HD 106906 (0.31; Crotts et al. 2021), although these comparisons are purely from empirical estimates

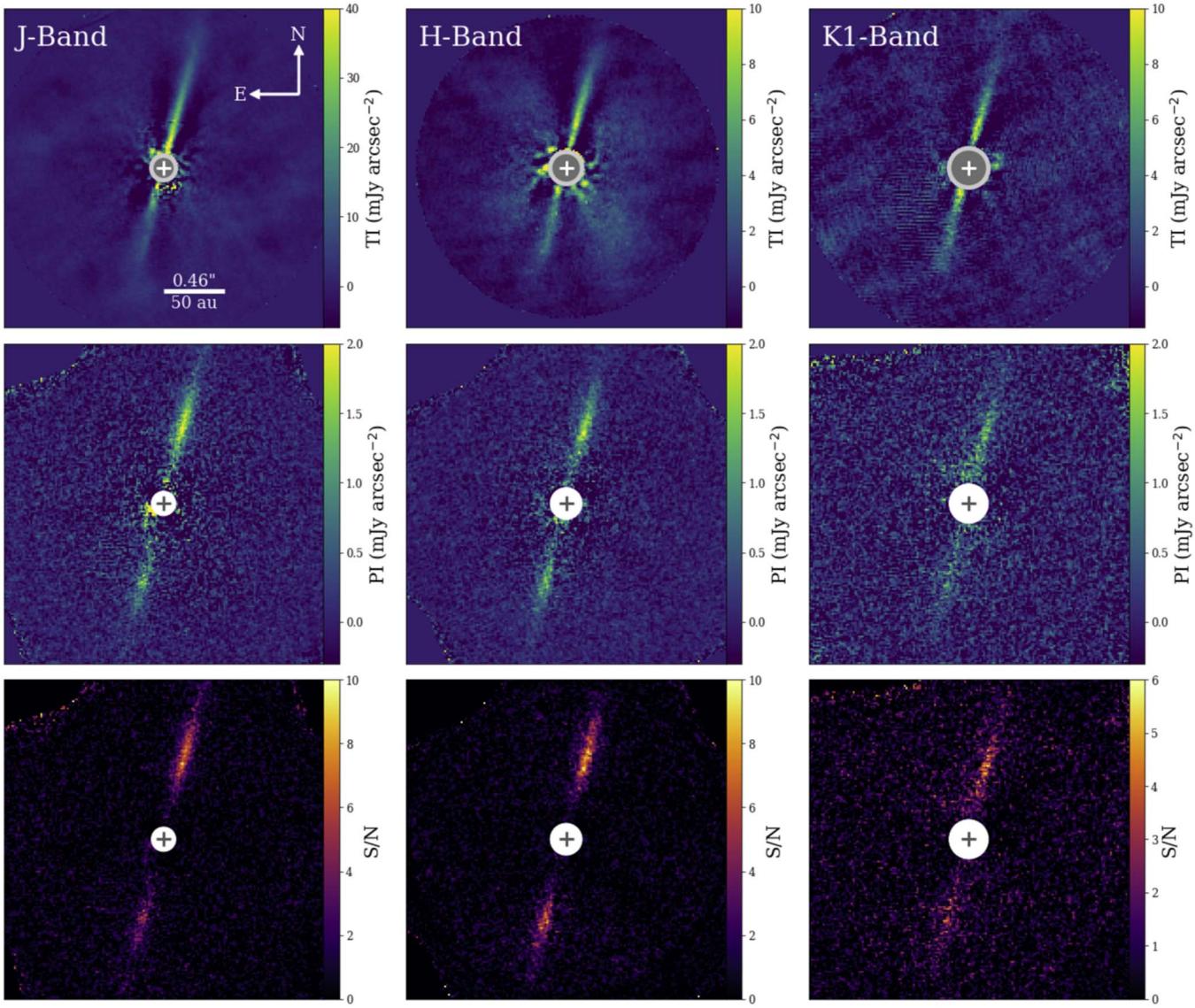

Figure 1. Top: the total intensity (TI) detections of HD 111520, produced by pyKLIP. Middle: polarized intensity (PI) of HD 111520. The polarized intensity is taken from the rotated stokes frame (Q_ϕ) to isolate the astrophysical emission. Bottom: S/N of the polarized intensity detections measured by dividing noise maps from the Q_ϕ data (see Section 2). The disk is consistently dimmer on the SE (left) extension of the disk compared to the NW (right) extension of the disk. The circles represent the size of the focal plane mask (0.″09, 0.″12, 0.″15 for *J*, *H*, and *K*1, respectively), and the crosses represent the location of the star. For all data, east is left and north is up.

and not from a proper disk model. A positive trend can be seen in the NW extension in all three bands, showing that the vertical width increases with radial distance on this side, while the SE extension is flat past 0.″6. This differs slightly from Draper et al. (2016), which only shows a positive trend in the NW extension past 0.″7. Additionally, an enhancement in the vertical width can be seen in the SE at a separation of ∼0.″5, strongest in the *H* and *K*1 bands, but also visible in the *J* band. A similar feature was observed in Draper et al. (2016), although we find this enhancement to be 0.″1 farther from the star. Given that the previous measurements were done with the total intensity *H*-band data, which are likely affected by PSF subtraction, our results using the polarized intensity are likely better to represent the true disk vertical width.

The vertical offset along the disk is small, with the largest offset being less than 0.″03, due to the disk being highly inclined. However, a clear offset can be seen in each band in Figure 2, showing that the disk inclination is not exactly 90°. In all three bands, the majority of data points are negative, indicating that the front side of the disk lies to the west, contrary to what is observed in Draper et al. (2016). We are also able to clearly detect a vertical offset in the SE extension, whereas the previous measurements in Draper et al. (2016) were unable to do so, showing the improvement that our polarized data have in measuring the vertical profile of the disk.

To further constrain the disk geometry, we fit the vertical offset or disk spine with a narrow, inclined ring model, similar to that used in Duchêne et al. (2020). We perform the fitting for all three bands, which will allow us to determine which parameters can be well constrained and which ones cannot. For the fitting procedure, MCMC via the Python package *emcee* (Foreman-Mackey et al. 2013) is utilized. Ring models are first generated from the equation of an ellipse with a given disk radii (R_d), *x* and *y* disk offset (δ_x, offset along the major axis, and δ_y, offset along the minor axis), disk inclination (*i*), and position angle (PA) measured from east to north through rotating the

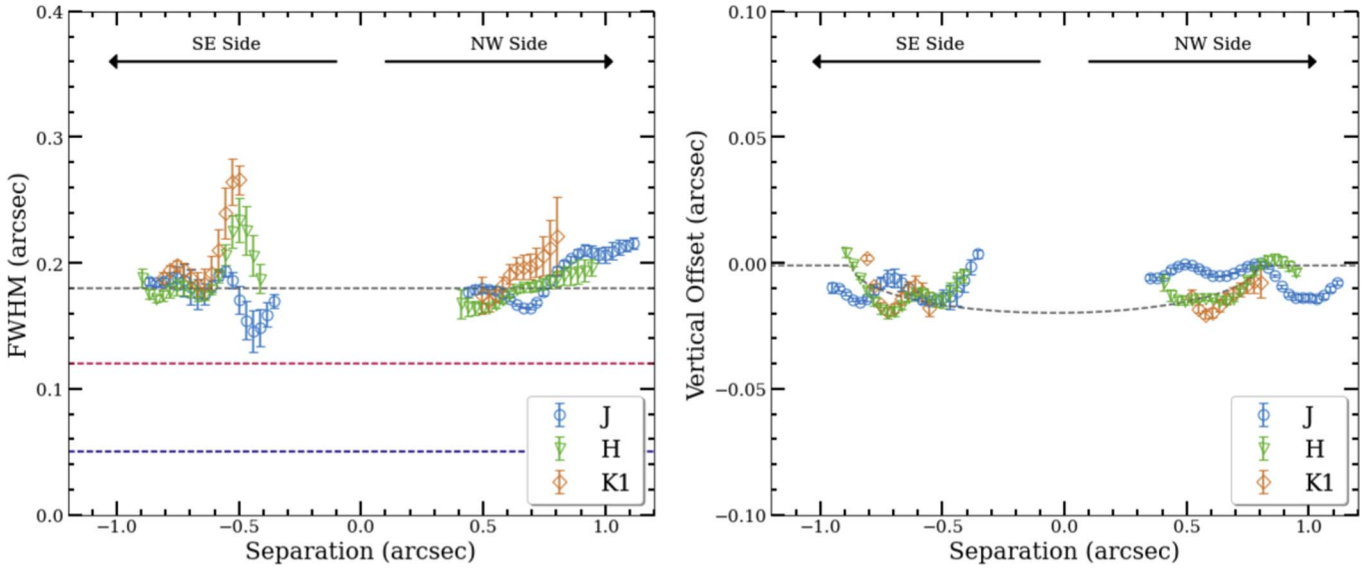

Figure 2. Left: the vertical width (FWHM) profile of HD 111520 as a function of separation from the star in each band. The gray horizontal dashed line represents the measured weighted FWHM, while the red line represents the intrinsic FWHM as measured in the H band. The dark blue line represents the FWHM of the GPI H-band PSF. Right: the vertical offset profile as a function of the separation from the star in each band. The dashed gray line represents the best fitting narrow ring model for the H band. For both profiles, we exclude measurements within 03 and greater than 1″ (with exception of the J band) due to low S/N.

Table 2
Measured Properties of the Vertical Profile for Each Band

Band	FWHM (″)	R_d (″)	δ_x (″)	δ_y (″)	i (°)	PA (°)
J	0.12 ± 0.01	$0.74^{+0.01}_{-0.01}$	$0.19^{+0.01}_{-0.01}$	$-0.009^{+0.001}_{-0.001}$	$89.43^{+0.03}_{-0.03}$	$165.06^{+0.01}_{-0.01}$
H	0.12 ± 0.01	$0.83^{+0.01}_{-0.01}$	$-0.04^{+0.01}_{-0.01}$	$-0.002^{+0.001}_{-0.001}$	$88.71^{+0.08}_{-0.06}$	$165.67^{+0.03}_{-0.03}$
$K1$	0.14 ± 0.01	$0.87^{+0.07}_{-0.04}$	$0.06^{+0.07}_{-0.04}$	$0.004^{+0.003}_{-0.003}$	$87.95^{+0.23}_{-0.23}$	$166.12^{+0.15}_{-0.18}$

Note. This includes the weighted intrinsic FWHM, along with the best-fit inclined ring model parameters.

data. Note that for the disk offsets, a negative value means a disk offset toward the left or down, while a positive value means a disk offset toward the right or up. These models are then compared to the data points using a χ^2 function. The results from this fitting procedure for all three bands can be found in Table 2.

Through this modeling, there are three parameters that we can better constrain: the inclination, PA, and δ_y. As expected, we find HD 111520's debris disk to have a very high inclination, no more than 2°.7 away from completely edge-on given 3σ uncertainties of the PA in the $K1$ band. Our measurement of the PA is also consistent with that measured in Draper et al. (2016), where we find it to lie between 165° and 166°. We find no significant offset along the minor axis (δ_y), with an offset of $\lesssim$0.″01. Taking into consideration the uncertainty in the position of star, which is 0.05 pixels (or ~0.7 mas) for GPI (Wang et al. 2014), makes this small offset negligible. Unfortunately, due to the high inclination of the disk, the disk radii, R_d, and offset along the major axis, δ_x, are too difficult to constrain from this type of modeling, and varies significantly between bands.

A possible warp is identified in Draper et al. (2016), where the SE extension was found to not align perfectly with the NW extension. However, such a warp is not seen in our vertical offset profiles. As a confirmation, we also check the vertical offset profiles for all three bands of the Spec data. Doing so, we find that this potential warp is also not present, showing that the warp feature is likely an artifact and a result of PSF subtraction in the H-band Spec data. This again shows that our higher S/N data greatly improves our measurements of the vertical profile and helps better constrain the disk's morphology and orientation.

3.2. Surface Brightness

Previous analysis of GPI observations for HD 111520 report a 2:1 brightness asymmetry in the H band (Draper et al. 2016). We measured the surface brightness of our multiwavelength data to better constrain the brightness asymmetry across all three bands, as well as to measure the disk color. Here, the vertical offset profile is used to approximate the peak surface brightness location along the disk. The surface brightness is integrated along 2 × 12 pixel bins at a series of radii from the star, where 12 pixels is similar to the measured FWHM of the disk. For the polarized intensity, 1σ uncertainties are measured using noise maps derived from the U_ϕ data in each band. In contrast, 1σ uncertainties for the total intensity are measured using the standard deviation of similar sized bins located at the same radial distance but outside the disk. We do not take into account the additional uncertainty in our total intensity data due to self-subtraction, as we are mainly interested in the brightness asymmetry between the two extensions, but note that this uncertainty exists. Figure 3 shows the final surface brightness as a function of separation from the star for all three bands in both polarized and total intensity. Only data points with an S/N $\geqslant$ 3 are plotted.

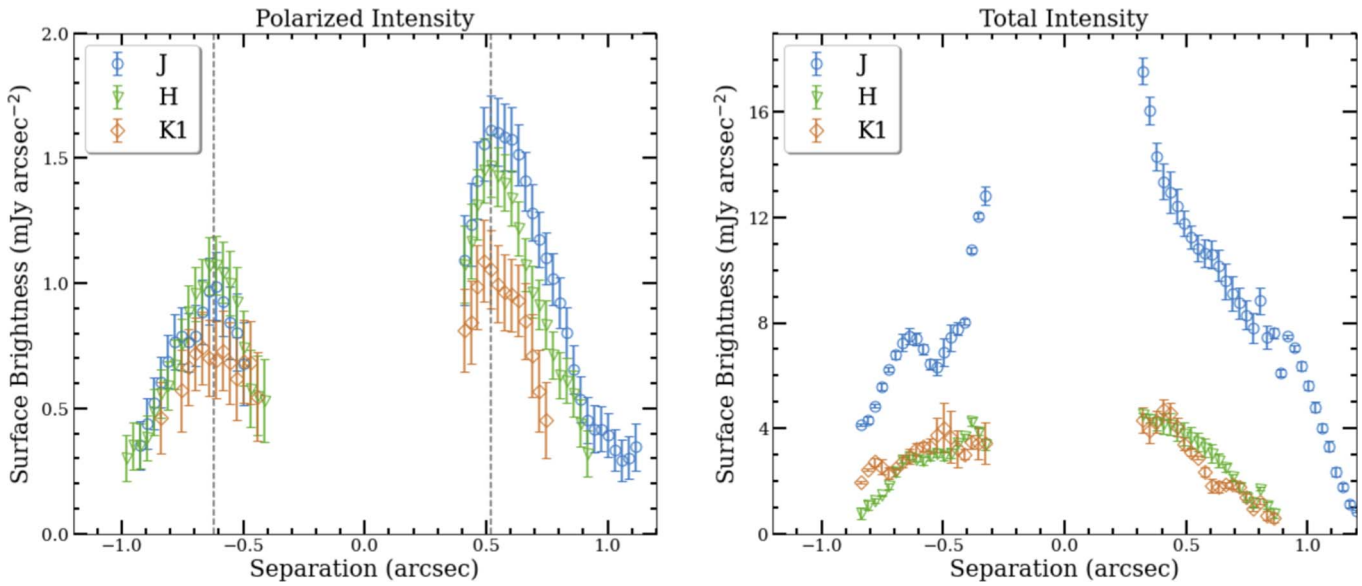

Figure 3. Left: the disk emission in polarized intensity as a function of separation from the star. The two vertical gray dashed lines represent the estimated location of the peak polarization on either side of the disk. Right: the disk emission in total intensity as a function of separation from the star. Disk orientation is the same as in Figure 2.

By eye, a stark difference between the polarized and total intensity surface brightness profiles can be seen. While the total intensity appears to peak either within or near the focal plane mask, and then consistently decreases with distance, the polarized intensity instead peaks at a farther separation on either side. This difference can be easily explained by the scattering phase function of the disk, where the total phase function should peak at small scattering angles due to strong forward scattering (Milli et al. 2017), while the polarized phase function should peak at larger scattering angles (Engler et al. 2017; Milli et al. 2019). Interestingly, the peak polarized intensity differs between the NW and SE extensions consistently between the three bands, where the NW extension peaks closer at $\sim 0\farcs52$ from the star compared to the SE extension, which peaks at a separation of $\sim 0\farcs62$ from the star (corresponding to a difference of $\sim$11 au). This suggests an eccentric disk with the NW extension located closer to the star compared to the SE extension.

Additionally, a clear brightness asymmetry can be seen in both polarized and total intensity. To probe the significance of this asymmetry, we compare the flux between the NW and SE extensions in all three bands. This is done by integrating the disk flux through two rectangular apertures (sized 30 $\times$ 15 pixels) placed on the NW and SE extensions at $0\farcs35$–$0\farcs8$ from the star, and then comparing the total integrated flux between the two sides. Uncertainties for the polarized intensity are measured by integrating the flux of the noise maps over the same aperture, while for the total intensity the uncertainty is measured by taking the standard deviation of the same sized aperture located at the same radius but placed outside the disk. The NW/SE integrated flux ratio for each band, Pol and Spec, can be found in Table 3. Our results show a similar trend between the polarized and total intensity with a large brightness asymmetry, most prominent in the J band, of $\sim$1.8:1, although not as large as the 2:1 asymmetry reported in Draper et al. (2016). What is more surprising is the apparent wavelength dependency of the brightness asymmetry, where the asymmetry seen in the H and $K1$ bands is significantly lower at only $\sim$1.5:1. We also find no brightness asymmetry at all in the $K1$-band total intensity, although this may be partially due to self-subtraction. Thus, the observed brightness asymmetry is strongest at shorter wavelengths and decreases as wavelength increases.

Table 3
Measured Brightness Asymmetry between the NW and SE Extensions (NW/SE) with 1σ Uncertainties

Mode	J	H	$K1$
Pol	1.77 ± 0.07	1.48 ± 0.05	1.45 ± 0.08
Spec	1.83 ± 0.01	1.44 ± 0.01	0.98 ± 0.01

Through the surface brightness in each band, we can also extract the disk's color, which can provide some information about its dust grain properties. This is because disk color is highly dependent on the scattering properties of dust grains, which are affected by composition, porosity, and grain size. For example, a blue disk color at NIR wavelengths can be caused by submicron-sized grains or very porous grains (Boccaletti et al. 2003). While it is difficult to disentangle these dust grain properties from the disk color alone, we would expect that the disk color should be the same across the disk given symmetrical dust grain properties. To measure the disk color, we use the same integrated flux used for measuring the brightness asymmetry. We then compare the integrated flux on both sides between each band, which are converted to magnitudes. Finally, given that these are scattered light observations, the stellar magnitude must be taken into account in order to measure the disk color. In this last step, the difference in magnitude of the star between each band is subtracted from the difference in disk magnitude between each band (e.g., $J - H = (J - H)_{\rm disk} - (J - H)_{\rm star}$). For the stellar magnitudes, we use the 2MASS J, H, and K magnitudes (8.00 ± 0.02, 7.83 ± 0.06, and 7.72 ± 0.02 mag, respectively; Cutri et al. 2003).

The derived disk colors can be found in Table 4. We include measurements for both polarized and total intensity for comparison, but note again that the total intensity data likely

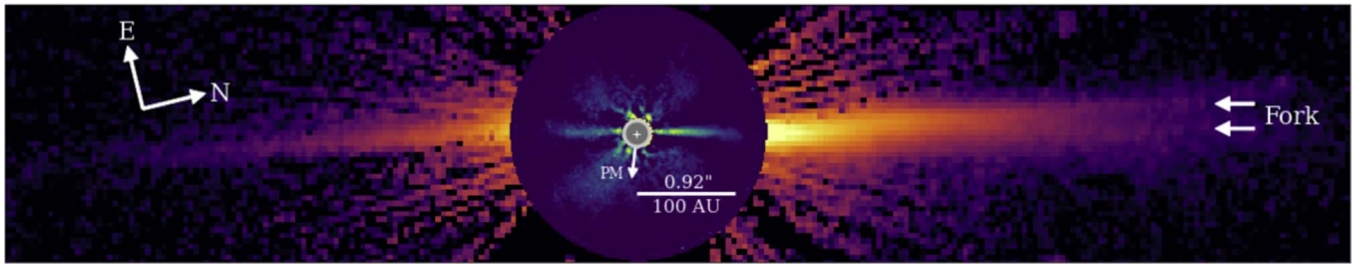

Figure 4. HD 111520 as seen by HST STIS (0.59 μm) and GPI (1.65 μm), both rotated by 75°.7 clockwise. The HST image is viewed in log scale. The southern extension is significantly dimmer than the northern extension, with brightness asymmetries of 1.5:1–1.8:1 within GPI's FOV and 5:1 in HST's FOV (Padgett & Stapelfeldt 2015). From GPI to HST scales, it is clear that there is a large-scale change in the disk. The south to north extension of the disk appears to have an asymmetrical geometry, with a possible bifurcation, or fork, seen on the northern side (Padgett & Stapelfeldt 2015). The central arrow represents the direction of the proper motion for the system.

Table 4
Measured Disk Color Using Polarized and Total Intensity, with 1σ Uncertainties

Bands	NW Extension (mag)	SE Extension (mag)
$J-H$ (pol)	-0.34 ± 0.03	-0.13 ± 0.05
$J-K1$ (pol)	-0.77 ± 0.04	-0.49 ± 0.06
$H-K1$ (pol)	-0.44 ± 0.04	-0.36 ± 0.06
$J-H$ (spec)	-1.59 ± 0.01	-1.17 ± 0.01
$J-K1$ (spec)	-1.77 ± 0.01	-1.16 ± 0.01
$H-K1$ (spec)	-0.18 ± 0.01	-0.01 ± 0.01

suffer from severe self-subtraction, and therefore provide less reliable measurements compared to the polarized intensity. These values show that the disk has a blue color at NIR wavelengths. However, what is even more interesting, is that the NW extension appears to be bluer than the SE extension in $J-H$ and $J-K1$, while the difference in color is still present but decreases significantly with $H-K1$ in both total and polarized intensity. This, along with the stronger asymmetry in the J band, suggests we are probing different dust grain properties at shorter wavelengths, a possibility that will be discussed further in Section 4.

3.3. HST Observations

While this paper is mainly focused on the micron-sized dust grains of the debris disk around HD 111520 as observed with GPI, we also take a deeper look into observations with HST STIS. HST data are sensitive to the smallest dust grains set on highly eccentric parabolic orbits by radiation pressure that form the most extended component of debris disks, also known as the disk halo (Hughes et al. 2018). These observations can be seen plotted in Figure 4, with the GPI data in the Spec H band plotted in the center. Like the dust grains observed with GPI, the disk halo also features strong asymmetries. This includes an even larger brightness asymmetry of 5:1, a radial asymmetry between the two sides, as well as a bifurcation or *fork* feature observed in the NW extension (Padgett & Stapelfeldt 2015; Draper et al. 2016). To probe the disk halo structure further, we measure the vertical offset of the HST STIS image in a similar manner as in Section 3.1; however, for the fork structure, we instead fit a double Gaussian profile instead of a single Gaussian profile. These results can be seen in Figure 5 along side the GPI vertical offset profile in the polarized H band for comparison.

What we find is that the disk halo appears to be warped, where beyond radial separations of $\sim 1''.7$, the vertical offset of the disk halo turns from being relatively flat and aligned with the GPI-imaged inner disk, to becoming sloped. While the SE extension warps downward, the NW extension slopes upward by roughly the same angle ($\sim 3°.8$). We are also able to resolve the vertical offset of the fork down to $\sim 2''.5$ and out to $6''$. The warp in the NW appears to align with the upper fork, while on the other hand, the GPI data appears to be aligned with the bottom fork. While there is a small uncertainty in the disk PA for both the GPI and HST STIS instruments of $\sim 0°.1$ each, this uncertainty does not change the alignment between the GPI data and the lower fork seen in the disk halo.

These results help clarify the disk morphology and show that the disk is being perturbed at large radial distances from the star. A planet companion as the potential cause for the warped structure and asymmetries of the disk halo will be addressed in Section 4.

4. Discussion

Through the analysis of HD 111520's disk structure, surface brightness, and disk color at multiple wavelengths, we have measured the disk's geometry, brightness asymmetry, and placed constraints on the dust grain properties. We find that the brightness and radial asymmetry is strongest in the J band and that the disk color of the NW extension is relatively bluer than the SE extension in $J-H$ and $J-K1$, while becoming more comparably blue in $H-K1$. This shows a possible wavelength dependence on all of the disk's observed asymmetries. As the disk color heavily depends on the dust grain properties, a difference between the color of the two extensions suggests we are probing different dust grain properties, either with the minimum dust grain size, composition, porosity, or a combination of these. The brightness asymmetry may also be explained by the disk eccentricity or an asymmetry in the dust mass distribution. In this section, we explore different scenarios by which the asymmetries and features seen in HD 111520 could have been formed given our results from the analysis of the GPI data, as well as the morphology of the disk halo observed with HST.

4.1. Disk Eccentricity

While it is difficult to derive information about a possible disk offset along the major axis through the vertical structure, given the high inclination, there is another clue that points toward the disk being eccentric. This includes the polarized intensity surface brightness profile, where we measure the

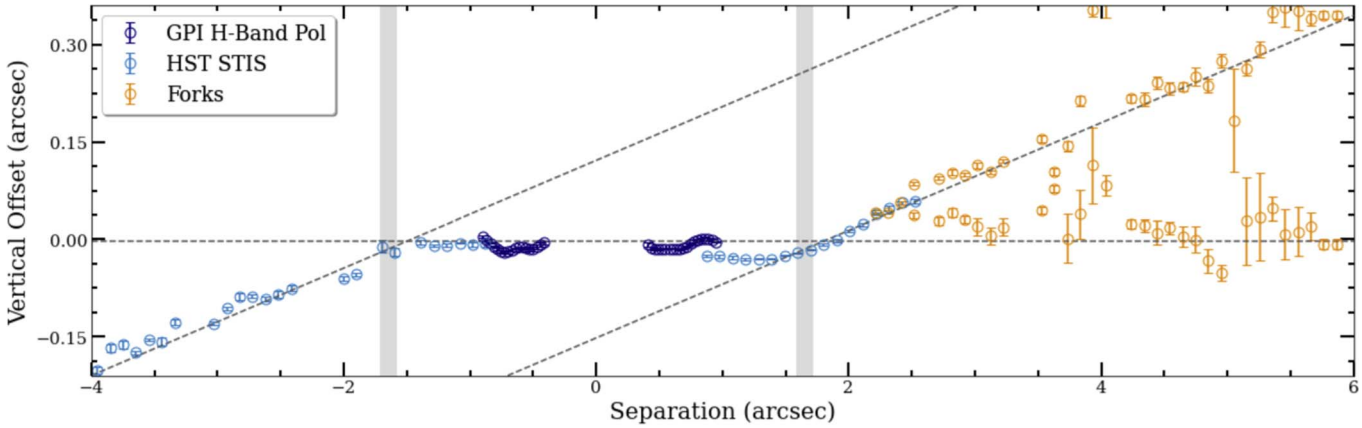

Figure 5. Vertical offset profiles of the GPI and HST data for HD 111520. Both images are rotated by 75.°7 clockwise. The dark blue data points represents the GPI vertical offset in the pol *H* band, the light blue data points represents the HST vertical offset, while the orange data points represent the vertical offset of the bifurcation or fork feature observed with HST in the NW extension. The diagonal gray dashed lines are plotted to show the slopes of the SE and NW extensions of the disk halo seen with HST, while the horizontal gray dashed line shows the alignment of the GPI data. The vertical shaded regions at 1.″7 show where the disk halo changes from being relatively flat to sloped.

brightness in the NW extension to peak closer to the star compared to the SE extension. In the case where there is no disk eccentricity, we would expect that the surface brightness would peak in the same location on either side. If the disk instead has some eccentricity, this would cause one side of the disk to be closer to the star, bringing the peak surface brightness of that side inwards and creating a pericenter glow (Wyatt et al. 1999; Pan et al. 2016). For HD 111520, this would mean that the NW extension lies closer to the star than the SE extension. If this is the case, this could at least partially explain the brightness asymmetry seen, as the NW extension would be receiving a higher amount of stellar light.

Given the separations of the two polarized peaks (∼0.″52/0.″62), we can place constraints on the possible eccentricity of the disk. Assuming that the argument of periapsis and the peak polarized intensity are both along the projected major axis, this leads to estimated eccentricity of 0.09. If the argument of periapsis is not along the projected major axis, the true eccentricity would be even larger making 0.09 a lower limit; however, this lower limit may be slightly overestimated if the peak polarized intensity is not along the projected major axis. Even so, such an estimated eccentricity is significant, and only observed in a handful of debris disks. One exciting aspect of these measurements is that an eccentric disk may point toward a hidden planetary companion, as planets on eccentric orbits have been shown to induce eccentric disks through dynamical simulations (Lee & Chiang 2016; Lin & Chiang 2019), as well as observations (e.g., Fomalhaut; Kalas et al. 2005; MacGregor et al. 2017). However, further analysis is required to see if an eccentric disk can fully explain the brightness and structural asymmetries observed.

As the surface brightness is related to $1/r^2$, with r being the radial separation from the star, we can also estimate what the brightness asymmetry should be given the different locations in the projected peak surface brightness. Taking the ratio of $1/r^2$ between the two sides, we find that a brightness asymmetry of ∼1.3:1 would be expected at a distance of between 0.″5 and 0.″6 from the star, assuming that the projected peak polarized intensity is occurring at the disk ansae. If in fact the projected peak polarized intensity is occurring elsewhere along the projected major axis, the expected brightness asymmetry would be even less. This is considerably lower than the 1.5:1–1.8:1 brightness asymmetry observed in the polarized intensity at these distances, meaning that while an eccentric disk may partially explain the observed brightness asymmetry, there must be another mechanism at play. This is further supported by the fact that, in the *J* band, the NW extension is much more extended than the SE extension, which should not be the case for an eccentric disk with a stellar offset toward the NW. Additionally, an eccentric disk alone would not explain the differences in brightness asymmetries we observe between bands, as well as the relatively bluer disk color observed in the NW extension. These inconsistencies again show that we need another phenomenon to help explain the disk's asymmetries.

4.2. ISM Interaction

Another possible explanation for the observed asymmetries is an interaction with the ISM. By passing through a dense ISM cloud, this can cause small dust grains in particular to be pushed toward the side of the disk opposite the direction of motion (Debes et al. 2009). This redistribution of small grains from one side of the disk to the other can cause one disk extension to become relatively brighter and more extended at shorter wavelengths, both of which we observe for HD 111520 with GPI. Similar features can be seen with HST, where the NW extension is brighter and more extended than the SE extension, as shown in Figure 4. If the NW extension is populated with smaller grains compared to the SE extension, this would also explain the much bluer disk color in the NW extension observed in $J-H$ and $J-K1$. However, for this to occur, the proper motion of the star must align in the correct direction. In the case of HD 111520, to create a NW extension that is brighter and bluer than the SE extension through an ISM interaction, the proper motion of the system must also be pointing toward the SE direction. The current measurements for HD 111520's proper motion are -35.3 mas yr^{-1} in R.A. and -16.7 mas yr^{-1} in decl. (Gaia Collaboration et al. 2021). Based on these measurements, this would mean that the proper motion is pointing toward the SW direction rather than the SE (see Figure 4), essentially ruling out an ISM interaction as the cause of the disk's color, radial, and brightness asymmetries.

4.3. Giant Impact

Another possible explanation of the features of HD 111520's debris disk would be a giant impact of two large bodies within the disk. Such an impact would generate an avalanche of small dust grains that would start out in a clump at the collision site, and would be redistributed throughout the disk over time. This scenario is consistent with the large brightness asymmetry observed and the difference in disk color, assuming that the impact occurred in the NW extension. A giant impact would have had to occur recently, on the order of a few thousand orbits (1 Myr at 50 au), in order for the pinched collision point to still be present, causing the observed asymmetries (Jackson et al. 2014). Because all particles are forced to pass through the collision point, this allows for further collisions and generation of small dust grains. After the collision point is smeared out, the asymmetry in the generated dust grains would start to become washed out due to collisional diffusion and blown out due to radiation pressure, returning the disk to an axisymmetric state over time. There are a few issues with this scenario, however. One issue is that typically the side opposite of the impact would be more radially extended (Jackson et al. 2014), whereas for HD 111520 we observe the opposite, although it is important to note that radiation pressure would also be playing a role in blowing out the small grains and we may not be sensitive to dust grains on the radially extended side, given the expected lower surface brightness. Another issue is that verification of this hypothesis is unfortunately not possible with GPI data alone.

Further evidence would include analyzing the dust mass distribution, which can be obtained through millimeter observations, as the majority of the observable disk mass lies within millimeter-sized dust grains and these grains are less susceptible to radiative forces in the disk. If the dust mass distribution in the millimeter-sized dust grains is also asymmetric, this would support a giant impact scenario and would help explain the very large surface brightness asymmetry. Higher resolution CO observations would also be extremely useful in this case, as a large impact may release a large amount of CO gas. If a concentration of CO is observed in the NW extension, this would help confirm the possibility of a giant impact as it has for the β Pic debris disk (Dent et al. 2014). While a marginally resolved continuum observation of the HD 111520 disk has been made with ALMA at 1240 μm (Lieman-Sifry et al. 2016), establishing an asymmetric dust mass distribution requires the disk to be well resolved. Along with the continuum, low resolution CO observations were also taken but no CO was detected. It is worth noting that there are several disks that are asymmetric in scattered light with symmetric millimeter-sized grains (HR 4796, HD 61005; Buenzli et al. 2010; MacGregor et al. 2018; Olofsson et al. 2019); however, such observations would still provide important information about the overall disk morphology. If there is an asymmetry in the millimeter-sized grains, then a local enhancement due to a large impact is likely, while symmetric millimeter-sized grains would support the need for an alternative mechanism to explain the asymmetries present in the scattered light in addition to an eccentric disk. Thus, high resolution ALMA observations of the millimeter continuum emission will be necessary in order to support or refute the hypothesis of a recent giant impact.

4.4. Disk Halo

In Section 3.3, our analysis of the HST observations revealed that the disk halo is warped past $\sim 1\farcs7$ on either side of the disk by $3\fdg8$. Additionally, the fork structure in the NW extension is resolvable from $2\farcs5$–$6''$. While the upper part of the fork is aligns with the warp of $3\fdg8$ in the NW extension, the lower fork is aligned with the inner part of the disk as observed with GPI. This alignment can rule out certain scenarios for the cause of the fork structure, such as self-shadowing from a higher dust mass in the NW extension as suggested in (Draper et al. 2016), which would require the larger grains to be aligned between the two forks.

One possible explanation for the fork's existence is that somewhere in the system exists an undetected planetary companion with a mutual inclination relative to the disk's. Such a planet has been shown to cause an "X" shape in the disk morphology in the dust density distribution, which may be observed as a fork like structure on either one or both sides of the disk depending on the viewing angle (Pearce & Wyatt 2014). However, this mainly applies to larger grains while smaller grains are also affected by radiation pressure, which may lead to a diminished effect. Such a planet may also cause the disk to become warped, such as the case with the inner disk of β Pic (Mouillet et al. 1997; Dawson et al. 2011; Apai et al. 2015). In the case of HD 111520, the warp observed would suggest a planet inclined at $\sim 3\fdg8$ relative to the disk, orbiting at a distance greater than $1\farcs7$ ($\sim$184 au) where the warp is observed. While dynamical modeling would be needed to place better constraints on a planet perturber, the complex structure of the disk halo does show that a planet companion at large separations likely exists in this system.

5. Conclusion

Using deep, multiwavelength GPI data of HD 111520's debris disk in both polarized and total intensity, we have been able to measure the disk's vertical structure, surface brightness profiles, and disk color.

1. We find that the disk has an intrinsic FWHM $0\farcs12$–$0\farcs15$ between the J, H, and $K1$ bands. The profile also exhibits a positive trend between the FWHM and radial distance in the NW extension, while in the SE extension an FWHM enhancement is observed at $\sim 0\farcs5$, which then flattens out past $0\farcs6$.
2. Measuring the vertical offset along the disk, we find that the west side is the front side of the disk. The measured disk spine also lies within $0\farcs03$ of the star location, showing the disk to have an inclination close to (but not quite) 90°. This is confirmed through modeling the vertical offset profile, where we derive an inclination roughly between 87° and 89° and a PA of 165°–166° from the best fitting models. We also derive disk offsets of δ_x and δ_y; however, the disk is too highly inclined to place a good constraint on the disk offset along the major axis. No disk offset is found along the minor axis.
3. Through characterization of the disk structure, we find a radial asymmetry exists, with an NW side that is more extended than the SE. However, this radial asymmetry is only present in the J band, while not present in the H and $K1$ bands.
4. By measuring the surface brightness in all three bands, we find that the polarized intensity and total intensity

have two very different profiles. Additionally, the polarized intensity peaks closer to the star in the NW extension compared to the SE extension, suggesting that the disk has an eccentricity of $\gtrsim$0.09. Although given an offset of $\sim$11 au along the projected major axis, this eccentricity would not be sufficient enough to be the sole cause of the disk's brightness asymmetry.

5. Comparing the surface brightness on either side shows a 1.5:1–1.8:1 brightness asymmetry, slightly less than what is observed in Draper et al. (2016). This asymmetry appears strongest in the J band and decreases with wavelength.
6. Similarly, measuring the disk color between each band in polarized intensity shows that the NW extension is relatively bluer than the SE extension in $J-H$ and $J-K1$, while this trend is not as strong in the $H-K1$ color.
7. Through measuring the vertical offset of the disk halo as seen with HST, we find that the small grains at large separations ($>1\farcs7$) are highly warped on either side. We also are able to measure the fork down to $\sim 2\farcs5$, where the GPI data appears to align with the lower fork.

Given the possibility of an eccentric disk, as well as the warped morphology of the disk halo, this suggests that there may be at least one planet perturber in this system, although dynamical modeling is needed to test this scenario. On the other hand, one way in which we can explain the large brightness asymmetry, as well as the difference in disk color between the two extensions, is if the two extensions contain differing dust grain properties, such as smaller grains in the NW extension. This can be caused by two scenarios: 1. An interaction with the ISM, or 2. a giant impact. While an ISM interaction would provide a straightforward explanation, the proper motion is not in the correct direction to account for the asymmetries between the NW and SE extensions. On the other hand, a recent giant impact between two large bodies may also be the source for the surface brightness and disk color asymmetries; however, further observations/evidence are needed to probe this scenario further. Specifically, a sub-arcsecond resolution image of the dust mass distribution and CO through higher resolution ALMA observations is essential.

HD 111520 serves as a very interesting and unique system to study, with such a large brightness asymmetry compared with other debris disks, as well as a complicated overall disk morphology. By studying the disk in greater detail, we can gain a greater understanding of the ways in which dynamical perturbations and collisions can affect disk morphologies, as well as how these types of debris disk systems evolve.

The authors wish to thank the anonymous referee for helpful suggestions that improved this manuscript. This work is based on observations obtained at the Gemini Observatory, which is operated by the Association of Universities for Research in Astronomy, Inc. (AURA), under a cooperative agreement with the National Science Foundation (NSF) on behalf of the Gemini partnership: the NSF (United States), the National Research Council (Canada), CONICYT (Chile), Ministerio de Ciencia, Tecnología e Innovación Productiva (Argentina), and Ministério da Ciência, Tecnologia e Inovação (Brazil). This work made use of data from the European Space Agency mission Gaia (https://www.cosmos.esa.int/gaia), processed by the Gaia Data Processing and Analysis Consortium (DPAC, https://www.cosmos.esa.int/web/gaia/dpac/consortium). Funding for the DPAC has been provided by national institutions, in particular the institutions participating in the Gaia Multilateral Agreement. This research made use of the SIMBAD and VizieR databases, operated at CDS, Strasbourg, France. We thank support from NSF AST-1518332, NASA NNX15AC89G, and NNX15AD95G/NEXSS. K.A.C. and B. C.M. acknowledge a Discovery Grant from the Natural Science and Engineering Research Council of Canada.

Facility: Gemini:South.

Software: pyKLIP (Wang et al. 2015), Gemini Planet Imager Pipeline (Perrin et al. 2014, http://ascl.net/1411.018), emcee (Foreman-Mackey et al. 2013, http://ascl.net/1303.002), corner (Foreman-Mackey 2016, http://ascl.net/1702.002), matplotlib (Hunter 2007; Droettboom et al. 2017), iPython (Perez & Granger 2007), Astropy (Astropy Collaboration et al 2018), NumPy (Oliphant 2006; https://numpy.org), SciPy (Virtanen et al. 2020; http://www.scipy.org/).

ORCID iDs

Katie A. Crotts https://orcid.org/0000-0003-4909-256X
Zachary H. Draper https://orcid.org/0000-0002-1834-3496
Brenda C. Matthews https://orcid.org/0000-0003-3017-9577
Gaspard Duchêne https://orcid.org/0000-0002-5092-6464
Thomas M. Esposito https://orcid.org/0000-0002-0792-3719
David Wilner https://orcid.org/0000-0003-1526-7587
Deborah Padgett https://orcid.org/0000-0001-5334-5107
Paul Kalas https://orcid.org/0000-0002-6221-5360
Karl Stapelfeldt https://orcid.org/0000-0002-2805-7338

References

Apai, D., Schneider, G., Grady, C. A., et al. 2015, ApJ, 800, 136
Astropy Collaboration, Price-Whelan, A. M., Sipőcz, B. M., et al. 2018, AJ, 1801, 02634
Boccaletti, A., Augereau, J. C., Marchis, F., & Hahn, J. 2003, ApJ, 585, 494
Buenzli, E., Thalmann, C., Vigan, A., et al. 2010, A&A, 524, L1
Crotts, K. A., Matthews, B. C., Esposito, T. M., et al. 2021, ApJ, 915, 58
Cutri, R. M., Skrutskie, M. F., van Dyk, S., et al. 2003, VizieR On-line Data Catalog: II/246
Dawson, R. I., Murray-Clay, R. A., & Fabrycky, D. C. 2011, ApJL, 743, L17
De Rosa, R. J., Nielsen, E. L., Blunt, S. C., Graham, J. R., & Konopacky, Q. M. 2015, ApJL, 814, L3
de Zeeuw, P. T., Hoogerwerf, R., de Bruijne, J. H. J., Brown, A. G. A., & Blaauw, A. 1999, AJ, 117, 354
Debes, J. H., Weinberger, A. J., & Kuchner, M. J. 2009, ApJ, 702, 318
Dent, W. R. F., Wyatt, M. C., Roberge, A., et al. 2014, Sci, 343, 1490
Draper, Z. H., Duchêne, G., Millar-Blanchaer, M. A., et al. 2016, ApJ, 826, 147
Draper, Z. H., Marois, C., Wolff, S., et al. 2014, Proc. SPIE, 9147, 91474Z
Droettboom, M., Caswell, T. A., Hunter, J., Firing, E., & Nielsen, J. H. 2017, Matplotlib/Matplotlib v2.0.2, Zenodo, doi:10.5281/zenodo.573577
Duchêne, G., Rice, M., Hom, J., et al. 2020, AJ, 159, 251
Engler, N., Schmid, H. M., Thalmann, C., et al. 2017, A&A, 607, A90
Esposito, T. M., Fitzgerald, M. P., Graham, J. R., et al. 2016, AJ, 152, 85
Esposito, T. M., Kalas, P., Fitzgerald, M. P., et al. 2020, AJ, 160, 24
Foreman-Mackey, D. 2016, JOSS, 1, 24
Foreman-Mackey, D., Hogg, D. W., Lang, D., & Goodman, J. 2013, PASP, 125, 306
Gaia Collaboration, Brown, A. G. A., Vallenari, A, et al. 2021, A&A, 649, A1
Hughes, A. M., Duchêne, G., & Matthews, B. C. 2018, ARA&A, 56, 541
Hung, L.-W., Duchêne, G., Arriaga, P., et al. 2015, ApJL, 815, L14
Hunter, J. D. 2007, CSE, 9, 90
Ingraham, P., Perrin, M. D., Sadakuni, N., et al. 2014, Proc. SPIE, 9147, 91477K

Jackson, A. P., Wyatt, M. C., Bonsor, A., & Veras, D. 2014, MNRAS, 440, 3757
Kalas, P., Graham, J. R., & Clampin, M. 2005, Natur, 435, 1067
Kalas, P. G., Rajan, A., Wang, J. J., et al. 2015, ApJ, 814, 32
Konopacky, Q. M., Thomas, S. J., Macintosh, B. A., et al. 2014, Proc. SPIE, 9147, 84
Lagrange, A.-M., Langlois, M., Gratton, R., et al. 2016, A&A, 586, L8
Lee, E. J., & Chiang, E. 2016, ApJ, 827, 125
Lieman-Sifry, J., Hughes, A. M., Carpenter, J. M., et al. 2016, ApJ, 828, 25
Lin, J. W., & Chiang, E. 2019, ApJ, 883, 68
MacGregor, M. A., Matrà, L., Kalas, P., et al. 2017, ApJ, 842, 8
MacGregor, M. A., Weinberger, A. J., Hughes, A. M., et al. 2018, ApJ, 869, 75
Macintosh, B. A., Graham, J. R., Palmer, D. W., et al. 2008, Proc. SPIE, 7015, 701518
Macintosh, B., Chilcote, J. K., Bailey, V. P., et al. 2018, Proc. SPIE, 10703, 107030K
Macintosh, B., Graham, J. R., Ingraham, P., et al. 2014, PNAS, 111, 12661
Maire, J., Ingraham, P. J., De Rosa, R. J., et al. 2014, Proc. SPIE, 9147, 85
Marino, S., Wyatt, M. C., Panić, O., et al. 2017, MNRAS, 465, 2595
Millar-Blanchaer, M. A., Graham, J. R., Pueyo, L., et al. 2015, ApJ, 811, 18
Milli, J., Engler, N., Schmid, H. M., et al. 2019, A&A, 626, A54
Milli, J., Vigan, A., Mouillet, D., et al. 2017, A&A, 599, A108
Mouillet, D., Larwood, J. D., Papaloizou, J. C. B., & Lagrange, A. M. 1997, MNRAS, 292, 896
Oliphant, T. E. 2006, A Guide to NumPy, Vol. 1 (Spanish Fork, UT: Trelgol Publishing)
Olofsson, J., Milli, J., Thébault, P., et al. 2019, A&A, 630, A142
Padgett, D., & Stapelfeldt, K. 2015, in IAU Symp. 314, Young Stars & Planets Near the Sun, ed. J. H. Kastner, B. Stelzer, & S. A. Metchev (Cambridge: Cambridge Univ. Press), 175
Pan, M., Nesvold, E. R., & Kuchner, M. J. 2016, ApJ, 832, 81
Pearce, T. D., & Wyatt, M. C. 2014, MNRAS, 443, 2541
Perez, F., & Granger, B. E. 2007, CSE, 9, 21
Perrin, M. D., Duchene, G., Millar-Blanchaer, M., et al. 2015, ApJ, 799, 182
Perrin, M. D., Maire, J., Ingraham, P., et al. 2014, Proc. SPIE, 9147, 91473J
Perrot, C., Thebault, P., Lagrange, A.-M., et al. 2019, A&A, 626, A95
Pickles, A. J. 1998, PASP, 110, 863
Rodigas, T. J., Hinz, P. M., Leisenring, J., et al. 2012, ApJ, 752, 57
Schmid, H. M., Joos, F., & Tschan, D. 2006, A&A, 452, 657
Schneider, G., Grady, C. A., Hines, D. C., et al. 2014, ApJ, 148, 59
Virtanen, P., Gommers, R., Oliphant, T. E., et al. 2020, NatMe, 17, 261
Wang, J. J., Ruffio, J.-B., De Rosa, R. J., et al. 2015, pyKLIP: PSF Subtraction for Exoplanets and Disks, Astrophysics Source Code Library, ascl:1506.001
Wang, J. J., Rajan, A., Graham, J. R., et al. 2014, Proc. SPIE, 9147, 55
Wolff, S. G., Perrin, M. D., Maire, J., et al. 2014, Proc. SPIE, 9147, 91477H
Wyatt, M. C. 2008, ARA&A, 46, 339
Wyatt, M. C., Dermott, S. F., Telesco, C. M., et al. 1999, ApJ, 527, 918